IOPscience iopscience.iop.org

Home Search Collections Journals About Contact us My IOPscience

Structural and electronic properties of epitaxial V_2O_3 thin films

This article has been downloaded from IOPscience. Please scroll down to see the full text article.

2004 J. Phys.: Condens. Matter 16 77

(http://iopscience.iop.org/0953-8984/16/1/008)

View the table of contents for this issue, or go to the journal homepage for more

Download details:
IP Address: 129.252.86.83
The article was downloaded on 27/05/2010 at 12:38

Please note that terms and conditions apply.

INSTITUTE OF PHYSICS PUBLISHING JOURNAL OF PHYSICS: CONDENSED MATTER

J. Phys.: Condens. Matter **16** (2004) 77–87 PII: S0953-8984(04)71054-1

Structural and electronic properties of epitaxial V_2O_3 thin films

B Sass[1], C Tusche[1], W Felsch[1], N Quaas[2], A Weismann[2] and M Wenderoth[2]

[1] I Physikalisches Institut, Universität Göttingen, Tammannstraße 1, 37077 Göttingen, Germany
[2] IV Physikalisches Institut, Universität Göttingen, Tammannstraße 1, 37077 Göttingen, Germany

E-mail: bsass@gwdg.de

Received 23 October 2003
Published 15 December 2003
Online at stacks.iop.org/JPhysCM/16/77 (DOI: 10.1088/0953-8984/16/1/008)

Abstract

Thin films of V_2O_3 with thickness 4–300 nm were grown on $(11\bar{2}0)$-oriented sapphire substrates by reactive dc magnetron sputtering. X-ray diffraction, pole figure measurements and scanning tunnelling microscopy show high crystallinity and epitaxy to the substrate with a faceted surface structure, and the absence of strain. Measurements of the electrical resistivity, scanning tunnelling and x-ray absorption spectroscopy show a metal–insulator transition near 150 K that is connected with the opening of an energy gap and a characteristic modification of the absorption spectrum at the vanadium-2p and oxygen-1s edges. These observations reveal that the $V_2O_3(11\bar{2}0)$ films have bulk-like properties.

1. Introduction

Vanadium sesquioxide is a fascinating material [1]. Strong electron correlation leads to a complex interplay of magnetism, structure and transport. Hybridization of the V-3d with the O-2p orbitals competes with a strong Coulomb interaction within the 3d shell (formal configuration $3d^2$ V^{3+}). Small perturbations in the balance of these effects by doping, deviations from stoichiometry, pressure or a change in temperature induce drastic modifications of the electronic properties, which are manifest in a very rich phase diagram [2–6]. Pure V_2O_3 at room temperature is a paramagnetic metal (PM). On cooling, a first-order transition to an antiferromagnetic insulating (AFI) phase occurs near 160 K, while Cr doping ($\sim$1%) transforms the PM at room temperature to a paramagnetic insulator (PI). At the PM to AFI transition an energy gap of $\sim$0.6 eV opens [7], the electrical resistivity increases by seven orders of magnitude [8], and the lattice symmetry transforms from rhombohedral (corundum) to monoclinic. The magnetic ordering pattern in the AFI phase is very peculiar and not that of a simple two-sublattice Néel configuration [9–11]: each V ion exchange coupling is ferromagnetic for V–V pairs along the *c*-axis and antiferromagnetic in adjacent $(11\bar{2}0)$ planes.

 © 2004 IOP Publishing Ltd Printed in the UK

The metal–insulator (MI) transitions have long been considered as classical examples of a Mott–Hubbard transition [12–14], but the complex interaction of the various electronic, magnetic and structural aspects posed major challenges for a theoretical understanding over years. Recently, a wealth of information on V_2O_3 has become available that gives new insight into this material. Examples to be mentioned are experimental data from polarized neutron scattering [15], resonant x-ray scattering [16, 17] and polarization-dependent V $L_{2,3}$-edge x-ray absorption spectroscopy [18] and photoemission [19]. The results have stimulated new theoretical work [20–26] that has considerably improved our understanding.

While the spectroscopic studies were mostly performed on bulk samples, the unusual properties of V_2O_3 have led to numerous efforts to grow thin films of this material [27–31]. Various qualities are documented. In the present paper we report on the structural and electronic properties of V_2O_3 layers we have grown on sapphire$(11\bar{2}0)$ substrates by reactive sputter deposition. The isotypic crystal structures of sapphire (α-Al_2O_3) and V_2O_3 favour epitaxial growth. This work provides the basis for a study of interfacial interaction effects in the bilayer systems Fe/$V_2O_3(11\bar{2}0)$ and Co/$V_2O_3(11\bar{2}0)$ across the metal–insulator transition of V_2O_3 presently under way in our laboratory [32]. Interfaces between insulating oxides and ferromagnetic metals are of great current interest, for example, in the context of spin tunnel [33] or exchange biased [34, 35] structures. A major problem encountered during preparation is that the window of the processing parameters for stoichiometric V_2O_3 films is relatively small. We demonstrate that a suitable choice of these parameters permits the growth, in a well controlled manner, of epitaxial layers of high quality with the properties of pure bulk V_2O_3. This is inferred from x-ray diffraction, measurements of the electrical resistivity and x-ray absorption spectroscopy (XAS) at the $L_{2,3}$ (2p $\rightarrow$ 3d) edge of V and the K (1s $\rightarrow$ 2p) edge of O. Scanning tunnelling spectroscopy (STS) reveals the opening of an energy gap at the MI transition, and scanning tunnelling microscopy (STM) the presence of a faceted surface structure with a preferred orientation perpendicular to the rhombohedral *c*-axis [0001].

The paper is organized as follows. We start with a brief description of the experimental methods employed (section 2). We then describe the various experiments carried out on V_2O_3 films grown on α-$Al_2O_3(11\bar{2}0)$ and discuss the results (section 3).

2. Experimental techniques

V_2O_3 films of thickness from 4 to 300 nm were deposited at normal incidence onto polished single crystalline sapphire substrates using reactive dc magnetron sputtering in normal incidence from a V metal target with 99.8% purity in an Ar–O_2 gas atmosphere. The substrates were $(11\bar{2}0)$ oriented with a miscut below 0.2°. Flow rates of Ar and Ar(90%)/O_2(10%) gases were individually controlled using a flow meter. The O_2 partial pressure was near 1% of the total process pressure adjusted to 3×10^{-3} mbar. The base pressure in the deposition chamber was 10^{-8} mbar. The substrates were preheated for 1 h at 600 °C, prior to deposition at this temperature. The dc power was set at 60 W leading to a growth rate of 0.26 nm s^{-1}.

Specular x-ray (Cu Kα) reflectivity data analysed with a simple kinematical scattering model (Parratt algorithm) has provided information on the thickness of the V_2O_3 films and their roughness. Structural characterization included symmetric Bragg reflection x-ray measurements (θ–2θ scans), x-ray diffraction rocking-curve and pole-figure measurements. Scanning tunnelling microscopy (STM) together with spatially resolved spectroscopy (STS) was performed *ex situ* using a variable temperature UHV instrument at both room and LN_2 temperatures. The data were recorded using tungsten tips after the surface had been cleaned by 2.5 keV Ar^+-ion bombardment. Constant current images were taken at a tunnelling current of 0.5 nA and a sample bias of 0.75 V. For convenient display a plane fit procedure was employed

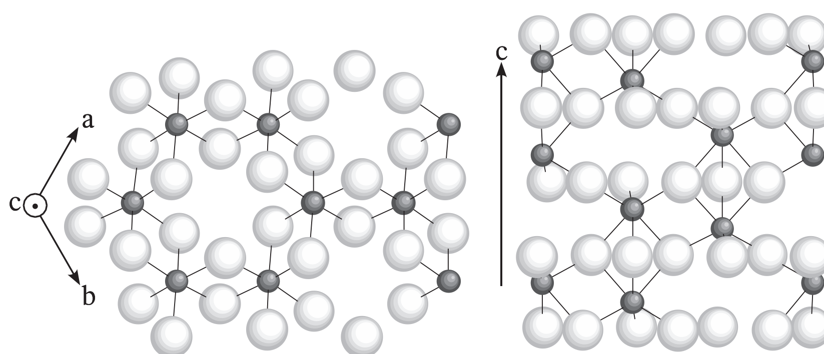

Figure 1. Projection of the (0001)-plane (left) and the (11$\bar{2}$0)-plane (right) in the rhombohedral corundum lattice of V_2O_3. The vanadium ions are represented by the small dark spheres.

for slope substraction. In the STS mode the bias voltage was varied from −1 to +1 V at a constant distance of several ångströms above the film surface. For each image of 80×80 nm^2 in size, 128×128 $I(U)$ curves were recorded. Standard four-point resistance measurements down to low temperatures have provided information on the quality of the metal–insulator transition of the V_2O_3 films.

The x-ray absorption (XA) spectra were acquired at the beamline SU23 of the SuperACO storage ring at the synchrotron radiation facility LURE in Orsay, France. The beamline supplies a monochromatic beam by a grating spectrometer with an energy resolution of 0.6 eV in the range of interest (500–900 eV), and circularly polarized light with a rate of 40% by an asymmetric wiggler. Electronic transitions from the V-2p and O-1s states into dipole allowed unoccupied states with d and p character, respectively, were studied. The spectra were obtained by measuring the photocurrent leaving the sample (total electron yield mode (TEY)) and thus are estimated to probe the top ∼5 nm of the layers. Prior to the XA measurements the sample surfaces were cleaned by repeated cycles of ion etching and annealing in the UHV preparation chamber of the beamline. The procedure removed VO_2 from the surface as evidenced by x-ray photoelectron spectroscopy (XPS). The overoxidization is due to air exposure since films analysed by XPS *in situ* after preparation showed the correct oxidation state.

3. Results and discussion

3.1. Structure

The rhombohedral corundum structure of bulk V_2O_3 (which is also that of sapphire) has an approximately hexagonal closed-packed array of oxygen ions in which the cations occupy two thirds of the octahedral sites (see figure 1). X-ray diffraction (XRD) Bragg scans for the V_2O_3 films on sapphire(11$\bar{2}$0) along the growth direction exhibit (11$\bar{2}$0) and (22$\bar{4}$0) reflections only (see figure 2). This indicates that the films are highly oriented, with the same orientation as the surface of the substrate. A rocking curve measured on the V_2O_3(11$\bar{2}$0) peak in figure 2 yields a full width at half maximum (FWHM) of 0.62°. The position of this peak located at $2\theta = 36.26°$ corresponds to the lattice parameter of the bulk material. The coherence length calculated from the FWHM agrees with the V_2O_3 film thickness measured by x-ray reflectivity. This implies that the film is in an out-of-plane coherent state.

The analysis of the in-plane alignment of the V_2O_3 film crystallites relative to the substrate was performed by XRD pole-figure measurements on the (10$\bar{1}$4) reflection. It was chosen for

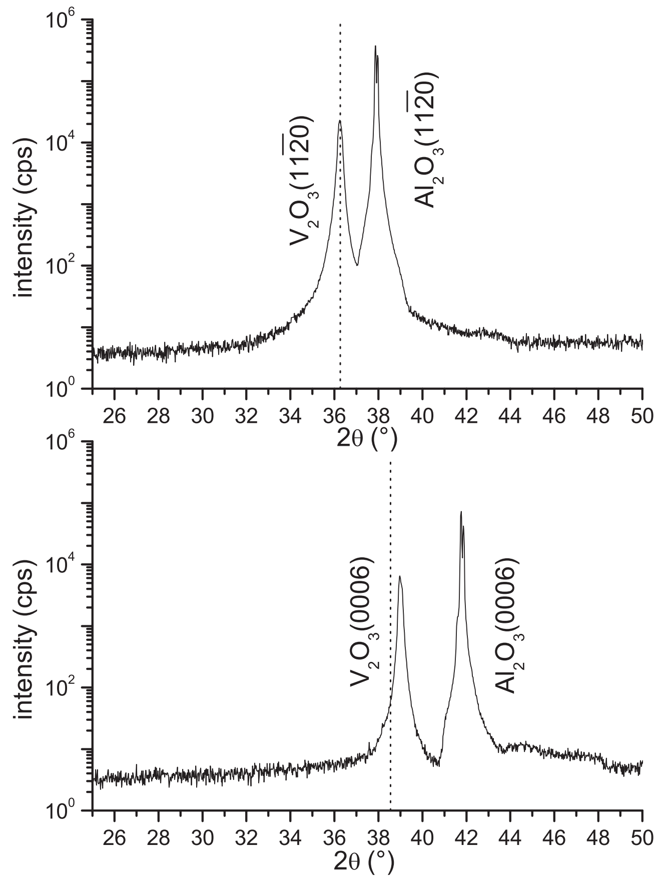

Figure 2. X-ray diffraction θ–2θ scans for 80 nm thick V_2O_3 films on (0001) and $(11\bar{2}0)$-oriented sapphire (α-Al_2O_3) around the main reflections $(11\bar{2}0)$ and (0006). The vertical line corresponds to the lattice parameter of the bulk V_2O_3.

its high intensity and easy distinction from other reflections. Figure 3 shows the contour maps obtained from a series of azimuthal (φ) scans by varying the tilt angle (ψ) at fixed incident angle $2\theta = 33.02°$. The spots observed at ($\psi = 56.8°$, $\varphi = 157.8°$) and ($\psi = 56.8°$, $\varphi = 337, 8°$) reveal complete epitaxy to the $(11\bar{2}0)$ surface of the sapphire substrate. Let us note that the epitaxial growth occurs in spite of the relatively large lattice mismatch between V_2O_3 and the substrate, of 7.8% along the [0001] direction (c-axis) in the $(11\bar{2}0)$ plane and 4.1% along the $[10\bar{1}0]$ direction (a-axis).

It has been reported [29] that V_2O_3 films epitaxially grown on (0001)-oriented sapphire substrates by reactive electron-beam evaporation are exposed to considerable strain. Variation of the growth parameters drastically modifies the properties of the V_2O_3 films, which in view of the sensitivity of the different phases of bulk V_2O_3 to pressure [4] the authors attribute to a varying degree of the strain. We have found that the general trend of the previous observations can be reproduced. It can be seen in figure 2 that oriented growth of V_2O_3 on the (0001) surface of sapphire can be achieved, but that the lattice parameter calculated from the position of the (0001) peak is distinctly smaller (by 1.2%) than that of bulk V_2O_3. This indicates considerable compressive strain in the layer along its normal. We shall show below (section 3.2) that the metal–insulator transition is suppressed in these films.

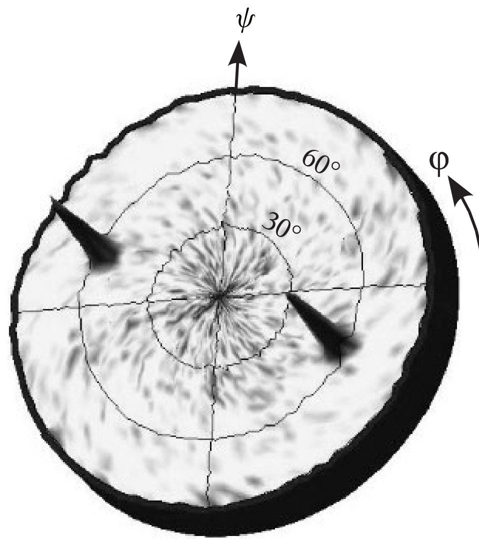

Figure 3. XRD pole figure measured for a 240 nm thick V_2O_3 film at fixed incident angle $2\theta = 33.02°$ corresponding to the $V_2O_3(10\bar{1}4)$ reflection. The intensity is displayed on a logarithmic scale. The background noise is three orders of magnitude lower than for the two spots.

The surface topology of the $V_2O_3(11\bar{2}0)$ films was characterized by STM. Figure 4 shows the topographic image of an 80 nm thick film at room temperature for a scan size of 400×400 nm^2. It exhibits a stripe-shaped microstructure elongated perpendicular to the c-axis, with an extension of 200 nm and width of 20 nm as typical dimensions. The root mean square (rms) roughness is about 1 nm, a value comparable to that derived from small-angle x-ray reflectivity. The self-organized faceted growth must be related to the anisotropic mismatch between the film and the substrate since the bare surface of the latter is structurally isotropic and smooth with a rms roughness below 0.14 nm. The width and roughness of the facets vary somewhat with the thickness of the films. There is no modification of the surface topology upon repeated cycling of the films across the metal–insulator transition.

3.2. Electrical resistivity

An important characteristic of the quality of the V_2O_3 films is the temperature dependence of their resistivity. Figure 5 shows the change of the resistance with temperature of two $V_2O_3(11\bar{2}0)$ films with different thickness and of a $V_2O_3(0001)$ film for comparison. The resistance of the $(11\bar{2}0)$-oriented films decreases linearly down to ~190 K as is expected for pure metallic V_2O_3. The resistivity at room temperature is comparable to the bulk value of 100 $\mu\Omega$ cm. Below ~160 K it increases steeply by several orders of magnitude, indicating the phase transition into the insulating state. The transition is fully reversible and shows hysteresis revealing that it is of first order. Compared to bulk V_2O_3 it is considerably broadened. This may be attributed to the interaction of the film with the substrate that hinders the structural transformation of the lattice from rhombohedral to monoclinic associated with the metal–insulator transition [28]. It can be seen in figure 5 that the effect is more pronounced at lower film thickness, where in addition to an increased broadening a reduced magnitude of the resistivity change is observed at the transition. It is interesting to note that for the $V_2O_3(11\bar{2}0)$

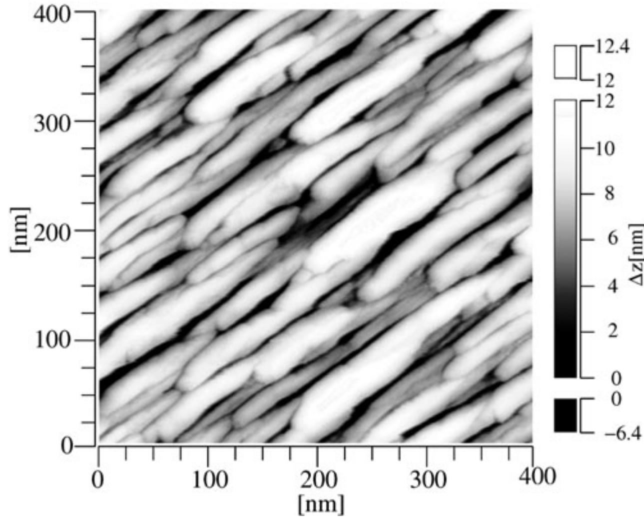

Figure 4. Topographic STM image of an 80 nm thick V_2O_3 film on $(11\bar{2}0)$-oriented sapphire at room temperature. The *c*-axis is directed along the diagonal of the image perpendicular to the stripes.

films with more bulk-like behaviour (thickness ~80 nm) the temperature of the metal–insulator transition, T_{MI}, can be systematically shifted by changing the oxygen partial pressure during deposition, i.e. T_{MI} is lowered for oxygen excess in agreement with the generalized phase diagram of bulk $V_2O_3(11\bar{2}0)$ [11, 36]. A prerequisite for this effect is low strain in the $(11\bar{2}0)$ oriented films.

As indicated above (section 3.1) it can be concluded from the x-ray diffractograms that the (0001)-oriented V_2O_3 films are exposed to considerable stress, in contrast to the $V_2O_3(11\bar{2}0)$ films. Figure 5 shows that this has a drastic effect on the electronic properties. The resistance shows thermally activated behaviour in the entire temperature range between 10 and 300 K with a change of five orders of magnitude. Selecting different film thicknesses and growing the films at different partial pressures of oxygen does not modify this behaviour qualitatively.

3.3. Scanning tunnelling spectroscopy

Topographic imaging by STM was combined with tunnelling spectroscopy probing the local $I(U)$ characteristics at different temperatures. In figure 6 we present the tunnelling current $I(U)$ and the corresponding differential conductance $\mathrm{d}I/\mathrm{d}U$ for a $V_2O_3(11\bar{2}0)$ film at two different temperatures. The spectra represent an average that was taken over the sample area shown in figure 7, which was recorded at 77 K. It is important to note that these topographic images do not change substantially when the films are cooled across the metal–insulator transition. This means that the formation of cracks due to the structural transformation that are frequently observed for bulk crystals (see, for example, [7]) can be excluded. The differences between the spectra in figure 6 are evident: at 300 K, i.e. above T_{MI}, we have metallic behaviour with a finite slope in the $I(U)$ characteristic at the Fermi energy, while at 77 K, below T_{MI}, $I(U)$ shows a plateau around E_F, typical of an energy gap of an insulator. The plateau can be seen particularly well in the $\mathrm{d}I/\mathrm{d}U$ curve and its width amounts to 0.45 ± 0.05 eV. This value compares favourably with the optical gap of 0.66 ± 0.05 eV obtained for a bulk stoichiometric V_2O_3 crystal with $T_{MI} = 159$ K [7]. The good agreement does not only demonstrate that the

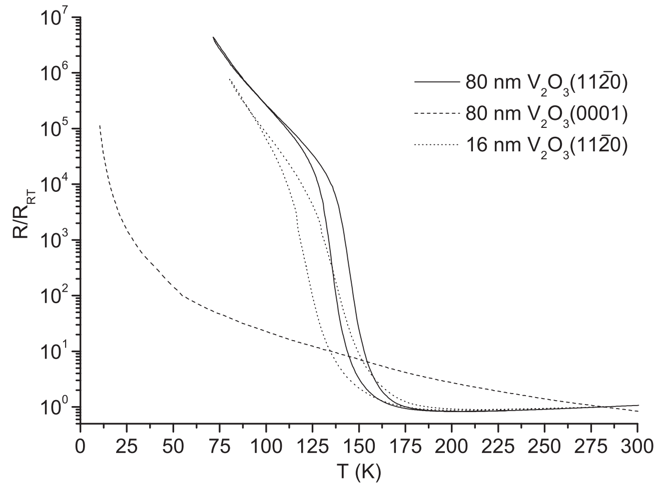

Figure 5. Resistance as a function of temperature, normalized to the value at room temperature, of two $V_2O_3(11\bar{2}0)$ films (thickness 16 and 80 nm) and of a $V_2O_3(0001)$ film (thickness 80 nm).

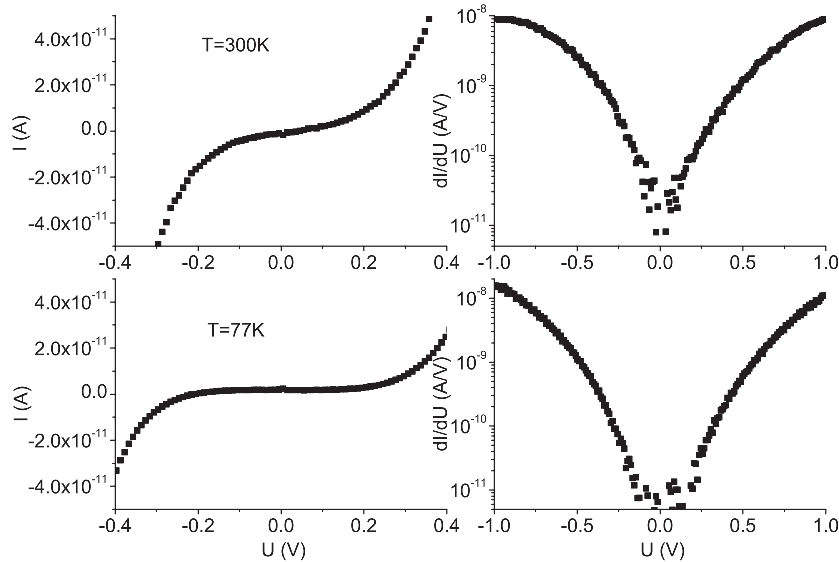

Figure 6. Tunneling current I and differential conductance $\mathrm{d}I/\mathrm{d}U$ versus bias voltage U for a $V_2O_3(11\bar{2}0)$ film (thickness 80 nm) at two different temperatures. The conductance $\mathrm{d}I/\mathrm{d}U$ is the numerical derivative of the $I(U)$ data. Note the different U scale of the $I(U)$ and $\mathrm{d}I/\mathrm{d}U$ plots. Note also the finite slope of $I(U)$ at $U = 0$ and $T = 300$ K, in contrast to $T = 77$ K.

metal–insulator transition reflected in the temperature dependence of the resistance (figure 5) even occurs at the surface of the $V_2O_3(11\bar{2}0)$ films, but it also implies that the surface clearly shows a metal–insulator transition similar to the bulk properties.

In order to probe the significance of this result and to visualize the local electronic structure we evaluated a 'gap map' from the $\mathrm{d}I/\mathrm{d}U$ versus U characteristics at 77 K over the complete area of the STM image in figure 7. The map is rather uniform: local gap values are close to the average extracted from figure 6, with only a few spots showing larger deviations. These

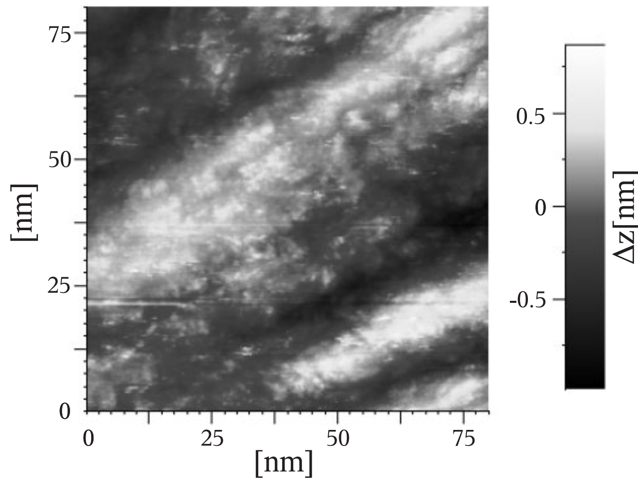

Figure 7. Topographic STM image of a $V_2O_3(11\bar{2}0)$ film (thickness 80 nm) at 77 K. The *c*-axis is directed along the diagonal of the image perpendicular to the facets.

spots are not correlated with the topography in a simple way, but are most likely due to defects resulting from surface preparation that are not resolved in the topographic image. In particular, no regions with metallic characteristics could be detected at this temperature. This fact finally justifies the averaging procedure we used to gain the spectra shown in figure 6 and lends confidence to the gap value estimate we extract from our STS measurement.

It seems that the electronic properties of the $V_2O_3(11\bar{2}0)$ surface differ clearly from those of the (0001) surface recently probed on a bulk single crystal [37]. The atomic ordering on the (0001) surface appears to depend sensitively on the surface preparation and may show reconstruction by dimerization of V atoms or not. Using STM and photoelectron spectroscopy (PES) it was found that only the dimerized surface develops a gap in the electronic density of states towards low temperatures. We have not checked the (0001)-oriented films because the metal–insulator transition is suppressed by strain.

3.4. X-ray absorption spectroscopy

Figure 8 displays the V 2p ($L_{2,3}$) and O 1s (K) x-ray absorption spectra of a V_2O_3 layer measured in the metallic (200 K) and insulating (50 K) states. The V related absorption extends to ∼530 eV, the O part lies above. Comparison of the overall spectral features with those of V_2O_3 single crystals [38, 39] reveals the following.

(i) The spectra represent electronic properties of *bulk* V_2O_3, i.e. the density of unoccupied states of d and p character at the V and O site, respectively, admixed into the low-lying conduction bands.
(ii) The modifications in the spectra seen upon crossing the metal–insulator transition agree with those previously observed [18, 39].

Recent experiments by polarization-dependent XAS [18] and theory [20, 24] have shown that a multi-band description of the electronic structure of V_2O_3 is essential in which the two 3d electrons of the V ion are distributed among a non-degenerate a_{1g} orbital oriented along the *c*-axis and a doubly degenerate e_g^{π} orbital oriented in the hexagonal plane. These orbitals derive from a splitting of the t_{2g} manifold of the V 3d states due to a small trigonal distortion

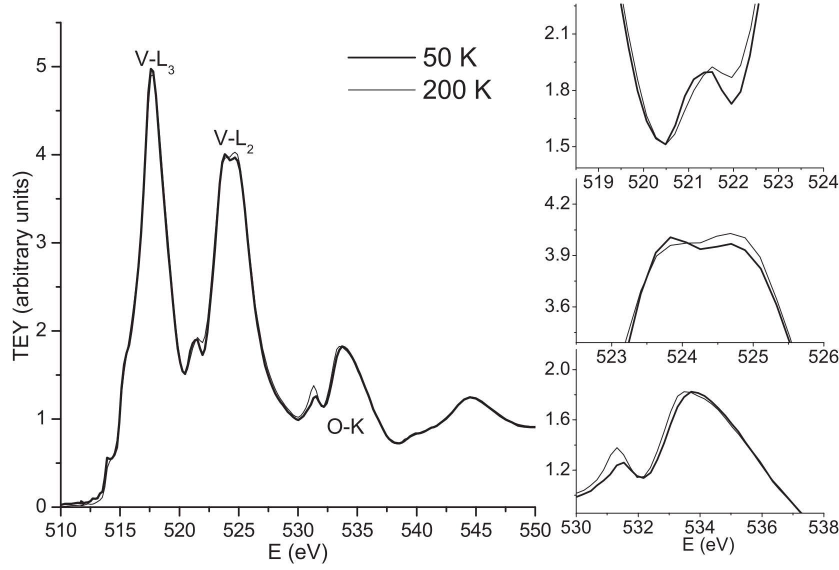

Figure 8. X-ray absorption spectra of a $V_2O_3(11\bar{2}0)$ film (thickness 80 nm) at the V-2p ($L_{2,3}$) and O-1s (K) edges measured in the metallic (200 K) and insulating (50 K) states.

of the octahedral crystal field set up by the O ions surrounding the V ions. Split off from these states and lying at higher energy is the unoccupied e_g^σ part of the V 3d states, as a result of the near octahedral symmetry of the crystal field. Important results of these studies are that the V ions are always in the high-spin $S = 1$ ground state favoured by the atomic Hund's rule and that the different phases of V_2O_3 have different orbital occupancies. The atomic configuration is an orbital mixture of $e_g^\pi e_g^\pi$ and $e_g^\pi a_{1g}$ configurations with different relative weight in the PM and AFI phases [18, 24]. The on-site 3d–3d Coulomb energy is spin and orbital dependent [18]. This connects variations in orbital occupation with changes of the intersite exchange interaction and of the band gap and effective bandwidth.

The spectra of the V_2O_3 layer in figure 8 are in good general agreement with those previously measured for bulk single crystals [18, 38, 39] in spite of the inferior photon-energy resolution (~0.6 eV) in the experiments reported here. Analysis of these results and comparison with theory [40–42] has permitted the authors to assign the different spectral features to the electronic structure. The line shape of the spin–orbit split V 2p ($L_{2,3}$) absorption spectrum reflects the final-state multiplet structure given by the Coulomb interaction between the 2p core hole and the 3d electrons, as well as by crystal-field effects [40–42]. Line shape and peak energies are sensitive to the chemical environment and can be used as a fingerprint of the V oxidation state. For example, the structure preceding the L_2 edge and the fine structure of the L_2 peak are typical of V^{3+} [38]. According to a recent calculation [24], the peak below the L_2 edge and the shoulder at the low-energy side of its maximum predominantly reflect contributions from the t_{2g}-derived a_{1g} and e_g^π states, respectively. The same assignment can be made to the two shoulders preceding the L_3 edge. The double-peak structure of the O K absorption spectrum is ascribed to the O p admixture to the crystal-field split V 3d states: the low-energy peak (~531.3 eV) to mixing with the t_{2g}-derived a_{1g} and e_g^π states, the peak at higher energy (~533.5 eV) to the e_g^σ states. Due to this hybridization the O 1s spectrum mainly maps the V 3d-band character and is sensitive to the metal–insulator transition (figure 8): in the AFI phase both peaks are shifted by ~0.3 eV to higher energy, and the peak at lower energy has

less spectral weight. The latter effect indicates a reduced hybridization of the unoccupied O 2p states with the V t_{2g} states relative to the hybridization with the V e_g^{σ} states. Modifications in the V 2p spectrum resulting from the metal–insulator transition appear essentially at the peaks of the L_3 and L_2 signatures and at the structures preceding them, the latter ones becoming more pronounced. These features may reflect the redistribution of states invoked by Park *et al* [18] to explain the linear dichroism and its variation across the phase transition in their XA spectra.

4. Conclusion

We have successfully grown epitaxial films of V_2O_3 with thicknesses from 4 to 300 nm on $(11\bar{2}0)$-oriented sapphire substrates. Various experimental techniques reveal that the physical properties of these films are close to those of the pure bulk crystals, even near the film surface: they have good crystallinity, are almost free of strain and show transitions from a metal to an insulator near 150 K. At the transition the electrical resistivity changes by nearly five orders of magnitude, and a gap opens in the electronic density of states near the Fermi energy, amounting to 0.45 eV at 77 K. Modifications of the x-ray absorption spectra at the 2p edge of vanadium and 1s edge of oxygen in the metallic and insulating states show the characteristic differences previously observed on bulk crystals [18, 39]. It is interesting to note that in the insulating phase the $V_2O_3(11\bar{2}0)$ films are antiferromagnetically ordered: the magnetization curve of a thin Co layer deposited onto their surface shows a pronounced exchange bias when the sample is cooled across the metal–insulator transition [32]. A typical feature of these films is self-organized growth with a faceted surface structure elongated perpendicular to the *c*-axis. This growth mode may be related to the anisotropic lattice mismatch with the substrate.

A limited complementary study on V_2O_3 films grown on (0001)-oriented sapphire with the same growth parameters reveals that they are highly oriented, too, but exposed to considerable strain, as noted before [29]. The metallic phase is suppressed in these films and electrical conduction was observed to be thermally activated over a temperature range of 10–300 K.

Acknowledgments

Helpful discussions with G Krill, F Bertrand, F Fortuna, Ph Ohresser and S Janicot, LURE, are gratefully acknowledged. We thank Y Luo for experimental support in the early stages of the sample preparation and T Scharf for the texture measurements. This work was supported by the Deutsche Forschungsgemeinschaft within SFB 602. It has benefited from the Access to Large Facilities Activity of the European Community's TMR Program. We thank the staff of beamline SU 23 at LURE for technical support.

References

[1] See, for example, Imada M, Fujimori A and Tokura Y 1998 *Rev. Mod. Phys.* **70** 1039
[2] McWhan D B, Rice T M and Remeika J P 1969 *Phys. Rev. Lett.* **23** 1384
[3] McWhan D B and Remeika J P 1970 *Phys. Rev.* B **2** 3734
[4] McWhan D B, Remeika J P, Rice T M, Brinkman W F, Maita J P and Menth A 1971 *Phys. Rev. Lett.* **27** 941
[5] McWhan D B, Menth A, Remeika J P, Brinkman W F and Rice T M 1973 *Phys. Rev.* B **7** 1920
[6] Kuwamoto H, Honig J M and Appel J 1980 *Phys. Rev.* B **22** 2626
[7] Thomas G A, Rapkine D H, Carter S A, Millis A J, Rosenbaum T F, Metcalf P and Honig J M 1994 *Phys. Rev. Lett.* **73** 1529
[8] Foex M 1946 *C. R. Acad. Sci.* B **223** 1126
[9] Moon R M 1970 *Phys. Rev. Lett.* **25** 527
[10] Word R E, Werner S A, Yelon W B, Honig J M and Shivashankar S 1981 *Phys. Rev.* B **23** 3533

[11] Bao W, Broholm C, Carter S A, Rosenbaum T F, Aeppli G, Trevino S F, Metcalf P, Honig J M and Spalek J 1993 *Phys. Rev. Lett.* **71** 766

[12] Mott N F 1968 *Rev. Mod. Phys.* **40** 677

[13] Mott N F 1990 *Metal–Insulator Transitions* (London: Taylor and Francis)

[14] Gebhardt F 1997 *The Mott Metal–Insulator Transition* (Berlin: Springer)

[15] Bao W, Broholm C, Aeppli G, Carter S A, Dai P, Rosenbaum T F, Honig J M, Metcalf P and Trevino S F 1978 *Phys. Rev.* B **58** 12727

[16] Paolasini L, Vettier C, de Bergevin F, Yakhou F, Mannix D, Stunault A, Neubeck W, Altarelli M, Fabrizio M, Metcalf P A and Honig J M 1999 *Phys. Rev. Lett.* **82** 4719

[17] Paolasini L, Di Matteo S, Vettier C, de Bergevin F, Sollier W, Neubeck W, Yakhou F, Metcalf P A and Honig J M 2001 *J. Electron Spectrosc. Relat. Phenom.* **120** 1

[18] Park J H, Tjeng L H, Tanaka A, Allen J W, Chen C T, Metcalf P, Honig J M, de Groot F M F and Sawatzky G A 2000 *Phys. Rev.* B **61** 11506

[19] Mo S K, Denlinger J D, Kim H D, Park J H, Allen J W, Sekiyama A, Yamasaki A, Kadono K, Suga S, Saitoh Y, Muro T, Metcalf P, Keller G, Held K, Eyert V, Anisimov V I and Vollhardt D 2003 *Phys. Rev. Lett.* **90** 186403

[20] Ezhov S Yu, Anisimov V I, Khomskii D I and Sawatzky G A 1999 *Phys. Rev. Lett.* **83** 4136

[21] Mila F, Shiina R, Zhang F C, Joshi A, Ma M, Anisimov V I and Rice T M 2000 *Phys. Rev. Lett.* **85** 1714

[22] Lovesey S W and Knight K S 2000 *J. Phys.: Condens. Matter* **12** L367

[23] Shiina R, Mila F, Zhang F C and Rice T M 2001 *Phys. Rev.* B **63** 144422

[24] Held K, Keller G, Eyert V, Vollhardt D and Anisimov V I 2001 *Phys. Rev. Lett.* **86** 5345

[25] Joshi A, Ma M and Zhang F C 2001 *Phys. Rev. Lett.* **86** 5743

[26] Di Matteo S, Perkins N B and Natoli C R 2002 *Phys. Rev.* B **65** 054413

[27] Case F C 1991 *J. Vac. Sci. Technol.* A **9** 461

[28] Rogers K D, Coath J A and Lovell M C 1991 *J. Appl. Phys.* **70** 1412

[29] Schuler H, Klimm S, Weissmann G, Renner C and Horn S 1997 *Thin Solid Films* **299** 119

[30] Guo Q, Kim D Y, Street S C and Goodman D W 1999 *J. Vac. Sci. Technol.* A **17** 1887

[31] Yamaguchi I, Manabe T, Kumagai T, Kondo W and Mizuta S 2000 *Thin Solid Films* **366** 294

[32] Sass B, Tusche C and Felsch W 2003 at press

[33] Prinz G A 1998 *Science* **282** 1660

[34] Nogués J and Schuller I K 1999 *J. Magn. Magn. Mater.* **192** 203

[35] Berkowitz A E and Takano K 1999 *J. Magn. Magn. Mater.* **200** 552

[36] Carter S A, Rosenbaum T F, Metcalf P, Honig J M and Spalek J 1993 *Phys. Rev.* B **48** 16841

[37] Preisinger M, Will J, Klemm M, Klimm S and Horn S 2001 *Preprint* cond-mat/0111113

[38] Zimmermann R, Claessen R, Reinert F, Steiner P and Hüfner S 1998 *J. Phys.: Condens. Matter* **10** 5697

[39] Müller O, Urbach J P, Goering E, Weber T, Barth R, Schuler H, Klemm M, Horn S and denBoer M L 1997 *Phys. Rev.* B **56** 15056

[40] de Groot F M F, Grioni M, Fuggle J C, Ghijsen J, Sawatzky G A and Petersen H 1989 *Phys. Rev.* B **40** 5715

[41] de Groot F M F, Fuggle J C, Thole B T and Sawatzky G A 1990 *Phys. Rev.* B **42** 5459

[42] de Groot F M F 1991 *PhD Thesis* University of Nijmegen